

Probing the structure of heterogeneous diluted materials by diffraction tomography

PIERRE BLEUET¹, ELÉONORE WELCOMME², ERIC DOORYHÉE³, JEAN SUSINI¹, JEAN-LOUIS HODEAU^{3*} AND PHILIPPE WALTER²

¹European Synchrotron Radiation Facility, BP 220, 38043 Grenoble Cedex, France

²Centre de Recherche et de Restauration des Musées de France, CNRS-UMR 171, Palais du Louvre, 14, quai François Mitterrand 75001 Paris, France

³Institut Néel, UPR 2940, CNRS, Université Joseph Fourier, 25 avenue des Martyrs, BP 166, 38042 Grenoble Cedex 9, France

*e-mail: hodeau@grenoble.cnrs.fr

Published online: 20 April 2008; doi:10.1038/nmat2168

The advent of nanosciences calls for the development of local structural probes, in particular to characterize ill-ordered or heterogeneous materials. Furthermore, because materials properties are often related to their heterogeneity and the hierarchical arrangement of their structure, different structural probes covering a wide range of scales are required^{1–23}. X-ray diffraction is one of the prime structural methods but suffers from a relatively poor detection limit, whereas transmission electron analysis involves destructive sample preparation. Here we show the potential of coupling pencil-beam tomography with X-ray diffraction to examine unidentified phases in nanomaterials and polycrystalline materials. The demonstration is carried out on a high-pressure pellet containing several carbon phases²⁴ and on a heterogeneous powder containing chalcodony and iron pigments. The present method enables a non-invasive structural refinement with a weight sensitivity of one part per thousand. It enables the extraction of the scattering patterns of amorphous and crystalline compounds with similar atomic densities and compositions. Furthermore, such a diffraction-tomography experiment can be carried out simultaneously with X-ray fluorescence, Compton and absorption tomographies⁶, enabling a multimodal analysis of prime importance in materials science, chemistry, geology, environmental science, medical science, palaeontology and cultural heritage.

Powder X-ray diffraction (XRD) is a major structural probe and is widely used to solve new crystalline structures, identify phases, estimate their mass fractions, analyse phase transformation and examine microstructural features. For heterogeneous samples, diffraction-based mapping experiments using a pencil beam have already been successfully applied for phase discrimination^{1–3}. These experiments provide a two-dimensional (2D) projection image of an object with a lateral resolution determined by the beam size, but they do not provide depth resolution. To overcome this intrinsic limitation, and in particular for a better understanding of ill-ordered materials, multidimensional and ultrasensitive imaging techniques are absolutely needed.

A pioneer development on the basis of wide-angle X-ray scattering computed tomography has been proposed for medical imaging^{4–6}. The concomitant availability of bright X-ray sources, high-resolution X-ray lenses and high-efficiency fast detectors offers a new favourable context for the development of high-resolution tomography-based techniques^{7–13}. Several other schemes

combining three-dimensional (3D) information and XRD at high spatial resolution have also been explored and successfully applied^{14–20}. It is worth noting that these latter methods have intrinsic limitations: first, they rely on assigned Bragg peaks on the basis of some *a priori* knowledge about the sample itself, and second, they are not applicable to ill-ordered or amorphous systems. At the nanometre scale, coherent diffraction imaging provides lensless morphological 3D images, that is, reconstructions of the inner density within nanocrystals, potentially coupled with lattice strains of known phases^{21–23}. Other methods on the basis of electron beams provide excellent lateral resolution but suffer from both a lack of depth resolution and a poor statistical sampling. Moreover, transmission electron analysis relies on complex and destructive sample preparation, which prevents analyses of precious samples.

In this paper, the high sensitivity and the high spatial resolution of X-ray diffraction computed tomography (XRD-CT) are demonstrated. XRD-CT is applied to phase mapping of unidentified nanocrystalline and powder crystalline materials. In addition to depth resolution and to non-invasive capabilities, this approach offers the possibility of recovering the local structural information after reconstruction using a reverse analysis.

To demonstrate the sensitivity of the technique, a sample containing several carbon phases with similar compositions or densities is selected. It results from the transformation of C₆₀ into diamond after high-pressure loading (close to 20 GPa) at room temperature²⁴. It was shown that, if compressed non-hydrostatically at room temperature, the fullerene cages are crushed into a mixture of polycrystalline cubic diamond and *sp*³ amorphous carbon²⁵. However this transformation is not yet completely elucidated and residual uncrushed C₆₀ molecules or 3D polymerized C₆₀ could not be isolated, although they were observed under different pressure and temperature conditions²⁶. The sample is analysed by direct XRD-CT: for each sample rotation ω and position y , 2D diffraction data are collected and transformed into a set of linear diffraction patterns (Fig. 1a,b). The stack of images is thus reduced to a 3D dataset whose dimensions are position y , tomographic angle ω and diffracted angle 2θ . To identify the major phases, a one-dimensional (1D) sum pattern is calculated by summing the linear diffraction patterns over y and ω . The linear diffraction patterns can be integrated along 2θ , and the result plotted as a function of the position y and tomographic angle ω to build up a so-called global

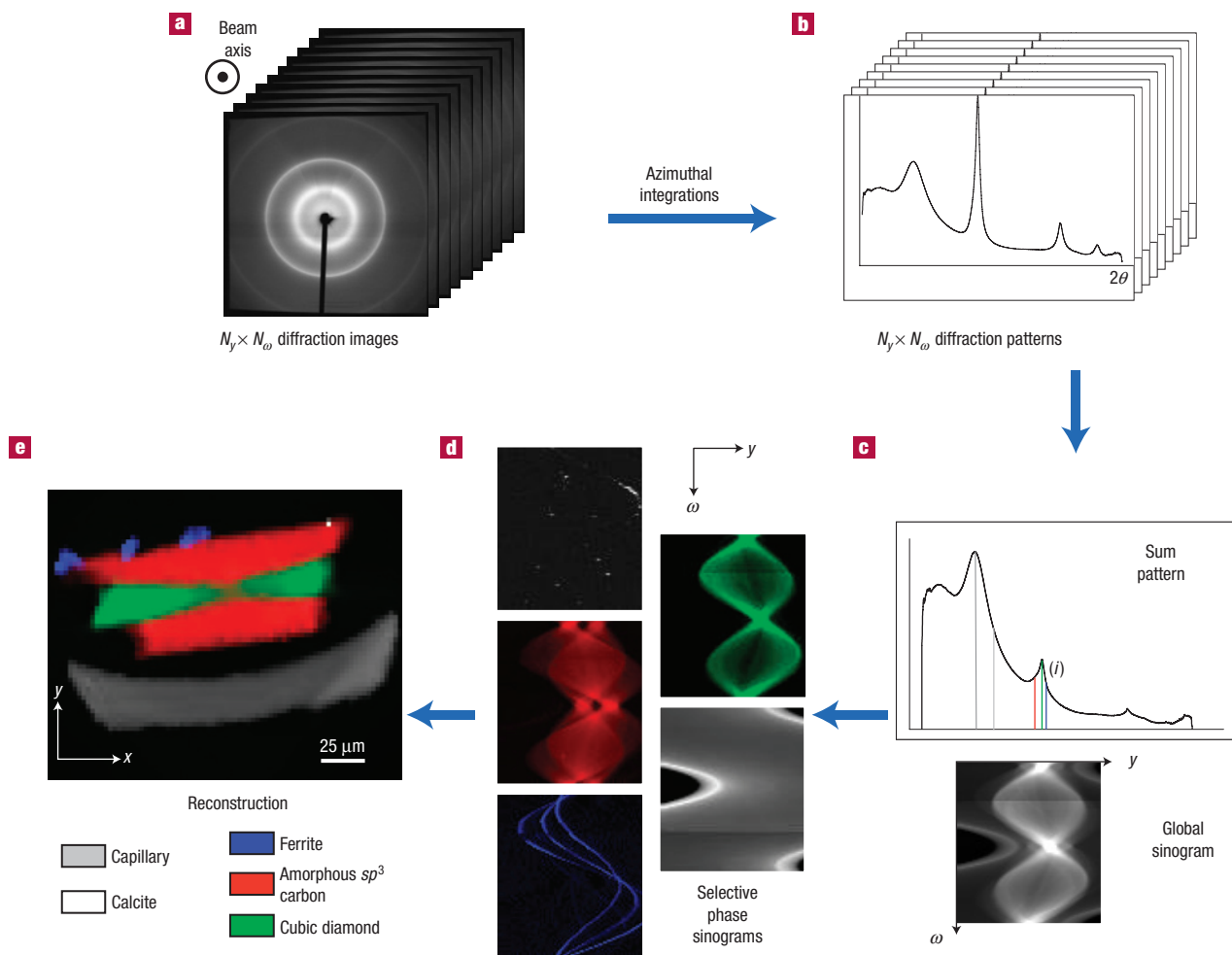


Figure 1 Diffraction–tomography direct analysis. The successive steps and principles of the reconstruction scheme of the XRD-CT direct analysis are illustrated with the phase identification of a C_{60} sample crushed under pressure²⁴. **a, b**, For every position (y, ω), the 2D scattering pattern (**a**) is integrated over the azimuthal angle and produces the respective 1D scattering pattern $f(2\theta)$ (**b**). **c**, On the one hand, all the 1D patterns are summed up over y and ω , to construct the scattering sum pattern of the entire sample. On the other hand, each 1D $f(2\theta)$ pattern is integrated over the diffraction angle 2θ , and the resulting total scattering intensity is plotted as a function of (y, ω) to build up the global sinogram. **d**, An ROI over any 2θ angle range, corresponding to a given scattering contribution or a diffraction peak (i), can be defined to extract the relevant sinogram of the corresponding individual phase. **e**, Finally, a reconstruction from these sinograms provides axial slices of the corresponding phases. This cross-section image reveals the spatial distribution of different phases: a butterfly necktie shape with a bright central part and an arc in the bottom part corresponding to the glass capillary.

sinogram (Fig. 1c), which is useful to reconstruct a cross-section of the whole diffracted intensity. A region of interest (ROI) can also be selected on the linear diffraction patterns to build up one sinogram over a particular 2θ range (Fig. 1d). For such an ill-ordered sample, the presence of amorphous phases and any possible peak overlap make difficult the selection of single Bragg peaks necessary for image reconstruction. Therefore, weighted sums of sinograms are computed using the PyMca software²⁷ to discriminate contributions from different phases. Five phases are identified and located with a detection limit better than 0.1%: two carbon phases with different crystallinities, the amorphous glass capillary container and two more unexpected contaminations at the sample periphery (Fig. 1d). Figure 1e shows one reconstructed (x, y) slice derived from the sinograms of Fig. 1d. Three grains of ferrite are isolated in the left upper part of the sample and one single grain of calcite at the top right.

A second major asset of XRD-CT is the possibility to carry out a reverse analysis to extract *a posteriori* the scattering/diffraction pattern from a selected area of the tomography image. Therefore, structural information such as lattice parameters, structure refinement, texture and grain size can be determined in an arbitrarily defined part of the sample, ultimately down to the voxel size. As shown in Fig. 2, the interpretation of a global XRD pattern of a complex multiphase system is often impaired by mixed contributions (phase and spatial distribution), which impedes the structural identification of trace phases. By using this reverse analysis, we overcome this limitation and recover single-phase patterns, including the patterns of any amorphous or diluted compounds (Fig. 2, A–E). The quality of the derived patterns makes the Rietveld simulation possible (Fig. 2, A'–D'). The Scherrer crystallite size of cubic diamond nanocrystals is extracted from the Rietveld fitting (4 nm) and the C–C bond length is estimated in

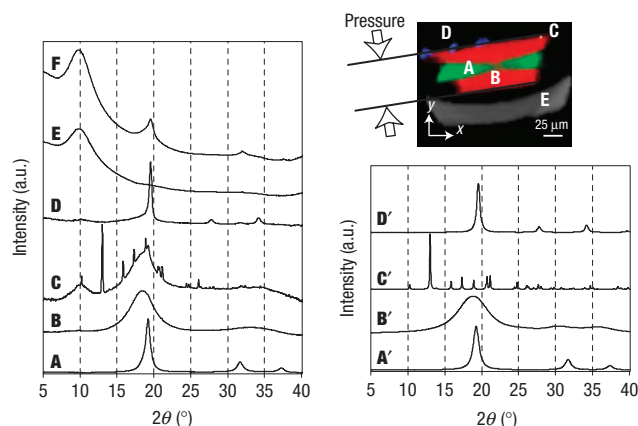


Figure 2 Diffraction–tomography reverse analysis. The patterns labelled A–E originate from the different phases shown in the colour image labelled A–E respectively. Pattern F is the scattering pattern of the whole sample derived from the sum of all measured y positions and ω orientations. The direction of pressure applied for sample synthesis, from C_{60} into carbon sp^3 phases, is indicated in the inset. A'–D' are the corresponding Rietveld calculated patterns used for phase-parameter determination: A and A', diamond C, cubic $Fd-3m$, $a = 0.35668$ nm, coherent grain size = 4 nm; B and B', amorphous C- sp^3 phase; B' is calculated using a 0.9 nm domain size and a cubic cell parameter $a = 0.371$ nm; it is worth noting that this phase corresponds better to an amorphous sp^3 phase as observed in amorphous Ge^{31,32} with C–C distances 4% larger than diamond C–C distances; C and C', calcite $CaCO_3$, trigonal $R-3c$, $a = 0.4991$ nm, $c = 1.7062$ nm; D and D', ferrite α -Fe, cubic $Im-3m$, $a = 0.28685$ nm, grain size = 7 nm; E, glass capillary container.

the pure amorphous sp^3 carbon phase (C–C = 0.161 nm) (Fig. 2, A', B'). Finally, the two minor impurity phases are fully identified and their structure can be refined (Fig. 2, C, C' and D, D').

The non-hydrostatic pressure at room temperature induces the formation of well-crystallized cubic diamond in the central part of the sample (A of Fig. 2), embedded within an amorphous carbon sp^3 phase matrix (B of Fig. 2). It is worth noting that neither uncrushed C_{60} nor polymerized C_{60} is found in the analysed volume. Furthermore, located at the sample surface, crystallized ferrite (α -Fe) grains are identified (D) as well as one single impurity grain of calcite ($CaCO_3$) (C), outlining the sensitivity of the method. Ferrite comes from some contamination by the razor blade during sample extraction whereas calcite is probably a dust particle in contact with the sample. The calcite grain occupies a single voxel. The reliability of the method is checked by observations of the same phase using ROIs over several (hkl) reflection peaks.

A third asset of XRD-CT is the possibility to combine simultaneously diffraction with fluorescence and absorption. This gives access to multimodal tomography as shown in Fig. 3 on a textbook powder with different grain sizes: a 300 μ m capillary is filled up with a mixture of chalcedony and iron pigments containing haematite (α - Fe_2O_3). Chalcedony is composed of long quartz microfibrils, generally less than 100 nm in diameter. As for the previous test case, a reverse analysis is carried out on this mixed powder. Even though chalcedony is by far the dominant phase (Fig. 4a,b), at least two types of iron grain are observed: haematite and siderite on the one hand, and haematite and phyllosilicate phases including greenalite on the other hand (Fig. 4c,d). For each grain, a diffraction diagram can be extracted from extremely tiny volumes of powder (as small as the voxel size), enabling subsequent data simulation or structural refinement.

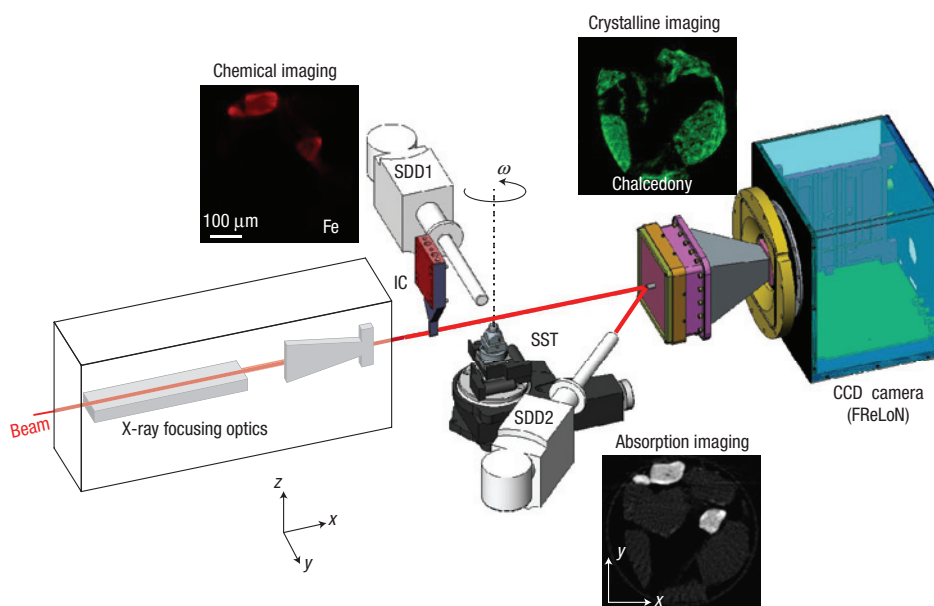


Figure 3 Diffraction–tomography set-up for a multimodal analysis. An 18 keV monochromatic X-ray beam is focused with a Kirkpatrick–Baez mirror system down to $1.6 \times 2.3 \mu m^2$ (vertical \times horizontal) with a flux of about 10^{11} ph s⁻¹. An energy dispersive detector (SDD1) placed at 90° to the incident beam direction measures the fluorescence signal. An ionization chamber (IC) measures the incoming I_0 intensity whereas a silicon drift detector (SDD2) collects the X-ray fluorescence I_F signal coming from a Ni foil placed on the beam stop behind the sample. The ratio I_F/I_0 is proportional to the absorption by the sample. A fast CCD (charge-coupled device) camera³³ collects the scattered/diffracted 2D patterns. The scanning scheme, ensured by a sample stage (SST), consists of a series of linear steps (y) associated with successive small rotations (ω) of the sample. Insets: the images of the chalcedony–Fe mixed-pigment sample are reconstructed from the XRD-CT direct computation using the various signals: X-ray absorption (bottom), Fe X-ray fluorescence (top left) and chalcedony diffraction (top right).

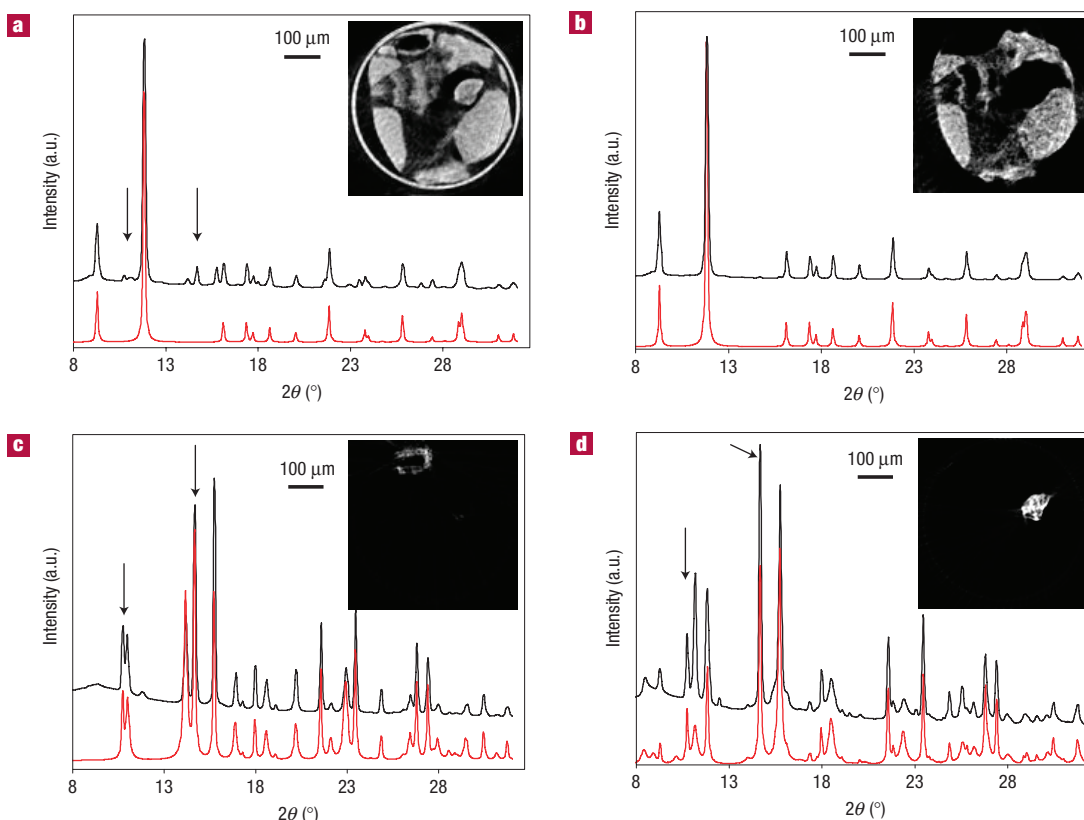


Figure 4 Phase-selective powder patterns and images. Experimental (black) and calculated (red) diffracted patterns and phase maps (insets) of the different phases extracted from a chalcedony–Fe-pigment powder, by using the XRD-CT reverse and direct analyses. **a**, Reconstructed XRD-CT image from the whole XRD diagram (black), compared with the calculated pattern of pure chalcedony (red). This shows that chalcedony is the major component in the powder. The main scattering contributions from the iron pigment are marked with arrows. **b**, Chalcedony, SiO_2 , trigonal $P3_121$, $a = 0.49134$ nm, $c = 0.54052$ nm; **c**, haematite, Fe_2O_3 , trigonal $R\text{-}3c$, $a = 0.50355$ nm, $c = 1.3747$ nm, and siderite, FeCO_3 , trigonal $R\text{-}3c$, $a = 0.46916$ nm, $c = 1.5379$ nm; **d**, haematite, Fe_2O_3 , trigonal $R\text{-}3c$, $a = 0.50355$ nm, $c = 1.3747$ nm, and greenalite, $\text{Fe}_3\text{Si}_2\text{O}_5(\text{OH})_4$, monoclinic $C2/m$, $a = 0.5390$ nm, $b = 0.9336$ nm, $c = 1.4166$ nm, $\beta = 90.01^\circ$.

The aim of the two described examples is to show the new opportunities offered by XRD-CT as a non-invasive structural analytical tool for heterogeneous materials. Phase-selective virtual cross-sections of unidentified bulk samples can be computed. No *a priori* knowledge about phases, crystallite orientations or atomic structure is required to carry out XRD-CT, on both/either well-crystallized and/or ill-crystallized materials. For this study, only computed 2D images have been considered, although a 3D reconstruction is a straightforward extension of the method by using a spiral scheme already validated for fluorescence tomography⁸. A global 3D scan of a $(100\text{ }\mu\text{m})^3$ volume, with a beam footprint size of $3\text{ }\mu\text{m}$, could be obtained in about 6 h. The high sensitivity of XRD-CT is due to the multiple collection of scattered patterns under the same experimental conditions but at different spatial and angular positions. Finally, for a representative sampling, the voxel size must match the microstructural features of the material, such as mosaicity and grain size. Given that modern hard-X-ray (sub)microprobes nowadays achieve 50–100 nm beams, the implementation of monochromatic submicro-XRD-CT could be tested, provided the sample is a nanocrystalline powder sample. The technique is not restricted to small beams but can also rely on larger beam, from the micrometre up to the millimetre range. It can also be extended to neutron radiation for diffraction analyses of large or highly absorbing heterogeneous bulk samples or for quantitative analysis of mixed amorphous phases.

The reverse analysis enables us to systematically extract the diffraction/scattering patterns of the pure diluted single phases from a complex mixture and opens the way to a powerful structural probe for heterogeneous materials. Moreover, it can be applied to either crystalline or amorphous phases even in the case of weak absorption or fluorescence contrasts. Another output is the possibility of *in situ* 3D phase distribution imaging. For example, the material structural heterogeneity in response to extrinsic temperature or pressure gradients can be studied. In such a case, the contribution of the *in situ* cell or container can be easily removed by computation. XRD-CT is fairly easy to handle by non-expert users and can benefit large communities. For instance, essential applications consist in the discrimination of polymorphic forms and textures in palaeontology, chemistry, medical sciences (calcified and lipidic tissues), materials science (nanorods, nanofoams, buckminsterfullerenes, nanotubes and so on) and biomineral studies (bones, teeth and shells²⁸).

XRD-CT fills the gap between the quantitative structural global probes, such as X-ray and neutron diffraction methods, and the local compositional probes, such as X-ray fluorescence and absorption computed tomographies or electron diffraction. Similarly to multimodal image fusion in medical imaging, this combination of X-ray absorption, fluorescence, diffraction and tomography will undoubtedly become an essential non-invasive analytical tool for researchers and engineers.

METHODS

BACKGROUND

Standard CT is based on absorption measurements while rotating a sample in the X-ray beam. Wide-angle X-ray scattering CT was first proposed for medical imaging^{4–6}. CT has recently been further extended using other X-ray–matter interactions such as phase contrast⁷, fluorescence^{8–11}, Compton scattering¹² or small-angle scattering¹³. With these techniques the morphology, the electron and mass densities and the major and minor chemical element distributions can be reconstructed numerically. In crystallized samples, three-dimensional images of the phase distribution are reconstructed using a set of conical slits with openings along the Debye–Scherrer diffraction cones, recorded by a 2D camera^{14,15}. X-ray structural 2D and 3D microscopy using polychromatic Laue diffraction is successfully applied on aluminium thin films and alloys^{16–18}. Microtomography can characterize 3D defect structure in bulk crystals^{19,20}. However, those methods rely on *a priori* knowledge about the sample and are not applicable to ill-ordered or amorphous systems. Using XRD-CT direct and reverse analyses, we can get a 3D structural mapping on one side, and selectively extract a pure pattern of an unknown part of a bulk sample on the other side.

PRINCIPLE

The XRD-CT principle consists in acquiring radial diffraction profiles in transmission with a 2D detector while translating (along y , perpendicularly to the beam axis) and rotating (ω) a sample illuminated by a pencil beam. Then, successive azimuthal integrations give a set of linear diffraction patterns (Fig. 1a,b); ROIs i corresponding to different (Bragg) angular intervals are selected to generate the so-called sinograms (Fig. 1c,d), which are a data representation $S^{i,z}(y, \omega)$ for the reconstruction at the height z of the sample. The reconstruction yields the variation of the intensity of any diffraction ROI as a function of (x, y, z) for each virtual section in the horizontal plane (Fig. 1e). To carry out this reconstruction, the standard algebraic reconstruction algorithm²⁹ is used. Because the XRD-CT geometry is fully compatible with detection of fluorescence and Compton signals, the diffraction measurements can be integrated into a more general multimodal strategy⁸, in which absorption, fluorescence, Compton and diffraction 2D or 3D images can be reconstructed simultaneously. Then, the reverse analysis consists of extracting the scattering/diffraction pattern from a selected area of the tomography image. The reverse analysis refers to the conversion of the $(x, y, 2\theta)$ scattering intensity distribution into conventional one-phased powder patterns. Two-dimensional (x, y) slices are reconstructed for each 2θ angle. This ends up with a stack of 2D images (as many as the number of 2θ data points in the linear patterns of Fig. 1b). From this, it is possible to generate a 1D profile along the 2θ axis for any given (x, y) voxel. The result is a pure diffraction/scattering pattern at this voxel, discarding the contributions of the surrounding voxels.

EXPERIMENTAL CONDITIONS

Measurements are made at the ID22 beamline³⁰ at the European Synchrotron Radiation Facility (ESRF, Grenoble, France). Samples are mounted inside a glass capillary. The energy of the monochromatic incoming beam is tuned at 18 keV. Using Kirkpatrick–Baez mirrors, the beam is focused down to the micrometre scale. The scan steps along y and ω are determined according to the probe size. The reconstruction algorithm provides an isotropic resolution of the reconstructed slice (x, y) , and the slice thickness is equal to the vertical beam size; the final voxel size is $2.3 \times 2.3 \times 1.6 \mu\text{m}^3$ in the present experiment. For optimal sampling and accurate unbiased diffracted intensities, the probe size must match a gauge volume containing a sufficiently large number of crystallites (several thousands). The length of the pencil beam in the sample can degrade the 2θ resolution because the sample is not a point source. Considering our 200 μm thick carbon sample and a maximum 2θ of 40° , it can be derived that the diffracted spot size is of the order of 130 μm , which corresponds to fewer than five pixels of our 2D camera (that is, $\Delta 2\theta = 0.06^\circ$). Because 2θ resolution broadening is more important for large Bragg angles, acquisition at a higher photon energy reduces this effect and also the sample absorption.

Received 26 October 2007; accepted 14 March 2008; published 20 April 2008.

References

- Manceau, A. *et al.* Deciphering Ni sequestration in soil ferromanganese nodules by combining X-ray fluorescence, absorption, and diffraction at micrometer scales of resolution. *Am. Mineral.* **87**, 1494–1499 (2002).
- Dooryhée, E. *et al.* Non-destructive synchrotron X-ray diffraction mapping of a Roman painting. *Appl. Phys. A* **81**, 663–667 (2005).
- Welcomme, E. *et al.* Classification of lead white pigments using synchrotron radiation micro X-ray diffraction. *Appl. Phys. A* **89**, 825–832 (2007).
- Harding, G., Kosanetsky, J. & Neitzel, U. Elastic scatter computed tomography. *Phys. Med. Biol.* **30**, 183–186 (1985).
- Harding, G., Kosanetsky, J. & Neitzel, U. X-ray diffraction computed tomography. *Med. Phys.* **14**, 515–525 (1987).
- Kleuker, U., Suortti, P., Weyrich, W. & Spanne, P. Feasibility study of x-ray diffraction computed tomography for medical imaging. *Phys. Med. Biol.* **43**, 2911–2923 (1998).
- Cloetens, P. *et al.* Holotomography: Quantitative phase tomography with micrometer resolution using hard synchrotron radiation x rays. *Appl. Phys. Lett.* **75**, 2912–2914 (1999).
- Golosio, B. *et al.* Nondestructive three-dimensional elemental microanalysis by combined helical x-ray microtomographies. *Appl. Phys. Lett.* **84**, 2199–2201 (2003).
- Kim, S. A. *et al.* Localization of iron in arabidopsis seed requires the vacuolar membrane transporter VIT1. *Science* **314**, 1295–1298 (2006).
- Larivière, P. J. & Vargas, P. A. Monotonic penalized-likelihood image reconstruction for X-ray fluorescence computed tomography. *IEEE Trans. Med. Imaging* **25**, 1117–1129 (2006).
- Schroer, C. G. Reconstructing x-ray fluorescence microtomograms. *Appl. Phys. Lett.* **79**, 1912–1914 (2001).
- Golosio, B., Brunetti, A. & Cesaero, R. Algorithmic techniques for quantitative Compton tomography. *Nucl. Instrum. Methods B* **213**, 108–111 (2004).
- Schroer, C. G. *et al.* Mapping the local nanostructure inside a specimen by tomographic small-angle x-ray scattering. *Appl. Phys. Lett.* **88**, 164102 (2006).
- Nielsen, S. F. *et al.* A conical slit for three-dimensional XRD mapping. *J. Synchrotron Radiat.* **7**, 103–109 (2000).
- Poulsen, H. F., Jensen, D. J. & Vaughan, G. B. M. Three-dimensional X-ray diffraction microscopy using high-energy X-rays. *Mater. Res.* **29**, 166–169 (2004).
- Tamura, N. *et al.* High spatial resolution grain orientation and strain mapping in thin films using polychromatic submicron x-ray diffraction. *Appl. Phys. Lett.* **80**, 3724–3726 (2002).
- Budai, J. D. *et al.* X-ray microdiffraction study of growth modes and crystallographic tilts in oxide films on metal substrates. *Nature Mater.* **2**, 487–492 (2003).
- Larson, B. C., Yang, W., Ice, G. E., Budai, J. D. & Tischler, J. Z. Three-dimensional X-ray structural microscopy with submicrometre resolution. *Nature* **415**, 887–890 (2002).
- Ludwig, W. *et al.* Three-dimensional imaging of crystal defects by ‘topo-tomography’. *J. Appl. Cryst.* **34**, 602–607 (2001).
- Ludwig, W., Lauridsen, E. M., Schmidt, S., Poulsen, H. F. & Baruchel, J. High-resolution three-dimensional mapping of individual grains in polycrystals by topotomography. *J. Appl. Cryst.* **40**, 905–911 (2007).
- Miao, J. *et al.* Three-dimensional GaN–Ga₂O₃ core shell structure revealed by X-ray diffraction microscopy. *Phys. Rev. Lett.* **97**, 215503 (2006).
- Pfeifer, M. A. *et al.* Three-dimensional mapping of a deformation field inside a nanocrystal. *Nature* **442**, 63–66 (2006).
- Miao, J., Ishikawa, T., Shen, Q. & Earnest, T. Extending the methodology of X-ray crystallography to allow structure determination of non-crystalline materials, whole cells and single macromolecular complexes (invited review). *Annu. Rev. Phys. Chem.* **59**, 24–27 (2008).
- Nunez-Regueiro, M., Monceau, P. & Hodeau, J.-L. Crushing C_{60} to diamond at room temperature. *Nature* **355**, 237–239 (1992).
- Hodeau, J.-L. *et al.* High-pressure transformations of C_{60} to diamond and sp^3 phases at room temperature and to sp^3 phases at high temperature. *Phys. Rev. B* **50**, 10311–10314 (1994).
- Marques, L. *et al.* Debye–Scherrer ellipses from 3D fullerene polymers: An anisotropic pressure memory signature. *Science* **283**, 1720–1723 (1999).
- Sole, V. A., Papillon, E., Cotte, M., Walter, P. & Susini, J. A multiplatform code for the analysis of energy-dispersive X-ray fluorescence spectra. *Spectrochim. Acta B* **62**, 63–68 (2007).
- Pouget, E. *et al.* Hierarchical architectures by synergy between dynamical template self-assembly and biomineralization. *Nature Mater.* **6**, 434–439 (2007).
- Natterer, F. & Wübbeling, F. *Mathematical Methods in Image Reconstruction* 110 (SIAM, Philadelphia, 2001).
- Somogyi, A. *et al.* ID22: A multitechnique hard X-ray microprobe beamline at the European Synchrotron Radiation Facility. *J. Synchrotron Radiat.* **12**, 208–215 (2004).
- Etherington, G., Wright, A. C. & Wenzel, J. T. A neutron-diffraction study of the structure of evaporated amorphous-germanium. *J. Non-Cryst. Solids* **48**, 265–278 (1982).
- Wright, A. C. *et al.* The structure of some simple amorphous network solids revisited. *J. Non-Cryst. Solids* **129**, 213–232 (1991).
- Labiche, J.-C. *et al.* The fast readout low noise camera as a versatile x-ray detector for time resolved dispersive extended x-ray absorption fine structure and diffraction studies of dynamic problems in materials science, chemistry, and catalysis. *Rev. Sci. Instrum.* **78**, 091301 (2007).

Acknowledgements

We wish to thank M. Nunez-Regueiro and L. Marques for sample synthesis, discussions and suggestions. The authors are also grateful to R. Tucoulou, S. Labouré, C. Guilloud, M. Soulier, Y. Dabin, C. Nemoz, J.-C. Labiche, A. Sole and the support groups of the ESRF for their help during experiments. This study was funded by grants from ESRF (LTP CH-1777).

Author information

Reprints and permission information is available online at <http://npg.nature.com/reprintsandpermissions>. Correspondence and requests for materials should be addressed to J.-L.H.